LAWRENCE
LIVERMORE
NATIONAL
LABORATORY

LLNL-JRNL-830795

In situ laser profilometry for material segmentation and digital reconstruction of a multicomponent additively manufactured part

D. J. Kline, M. D. Grapes, R. Chavez Morales, G. C. Egan, J. D. Sain, Z. D. Doorenbos, H. E. Fletcher, E. A. Avalos, B. M. English, V. Eliasson, K. T. Sullivan, J. L. Belof

January 12, 2022

Additive Manufacturing

Disclaimer

LLNL-JRNL-830795

IN SITU LASER PROFILOMETRY FOR MATERIAL SEGMENTATION AND DIGITAL RECONSTRUCTION OF A MULTICOMPONENT ADDITIVELY MANUFACTURED PART

Dylan J. Kline[1]*, Michael D. Grapes[1], Rodrigo Chavez Morales[2], Garth C. Egan[1], John D. Sain[1], Zachary D. Doorenbos[1], Hannah E. Fletcher[1], Eric A. Avalos[1], Benjamin M. English[1], Veronica Eliasson[2], Kyle T. Sullivan[1], and Jonathan L. Belof[1]

[1]Lawrence Livermore National Laboratory, Livermore, CA 94550, USA
[2]Colorado School of Mines, Golden, CO 80401, USA
*Corresponding author: kline11@llnl.gov

ABSTRACT

In addition to its ability to produce geometrically complex parts, additive manufacturing offers a unique opportunity to collect data about a component while it is being fabricated. However, there has only been limited effort to characterize parts morphologically and compositionally *in situ*. In this article, we present a layer-by-layer, laser profilometry-based *in situ* characterization technique as a method to digitally reconstruct a multi-material part. Data collected by the laser profilometer yields height maps and grayscale images which are voxelized using purpose-built software to volumetrically reconstruct the part. The same part was also analyzed using X-ray computed tomography (CT) which was not able to resolve the different compositional regions within the part, but captured the filament morphology. The part was then bisected to compare the digital reconstruction to the actual part morphology and composition. Overall, the digital reconstruction was in good agreement with both the CT and bisected images. Deviations between the digital reconstruction and the CT/bisected images are likely the result of image segmentation settings or material shifts after data was collected. The *in situ* characterization method demonstrated here sets the stage for real time process monitoring and paves the way for additively manufactured parts that are “born qualified.”

Keywords: *in situ* inspection, diagnostics development, machine vision, reconstruction, direct-ink-write.

1. INTRODUCTION

Over the last few decades, additive manufacturing has led to a paradigm shift in the fabrication of parts with increasingly complex geometries.[1] While additive manufacturing encompasses techniques like fused filament fabrication (FFF, typically for polymers) and powder bed fusion (for metals), perhaps the most versatile technique is direct ink writing (DIW).[1,2] DIW techniques use a flowable material which is extruded through a moving nozzle at a prescribed rate. DIW has been of particular interest for fabrication of architected parts with different and/or varied chemical properties.[3–10]

Despite the increasing versatility in manufacturing capabilities, part qualification and process monitoring have been long-standing challenges for most additive manufacturing techniques.[11,12] When the interior microstructure of a part is of interest, the most powerful method available for non-destructive characterization is X-ray computed tomography (CT), whereby X-ray image “slices” are stacked to form a volume.[13–15] However, CT scans can be time consuming (minutes to hours depending on the desired size and resolution) and thus only a small subset of a production run of parts might be inspected for acceptance. Furthermore, X-ray CT can only discriminate between materials with different attenuations and therefore may not be a suitable technique for components which have similar physical properties but different chemical properties.[13–15] In contrast, a reconstruction created from data collected during the additive manufacturing process can potentially be generated for every single part in a production run with minimal time penalty.

Considering that additive manufacturing gives native visual access to a part during its fabrication, some recent research has focused on *in situ* monitoring of additive manufacturing processes. A review article by Grasso et al. detailed multiple methods for collecting data *in situ* for metal additive manufacturing processes.[12] In their review, they classify different "levels" of *in situ* monitoring for metal additive manufacturing ranging from 0-4 which include (0) fabrication device measurements, (1) layer-wise measurements of the part, (2) byproduct measurements from shortly behind the build path, (3) measurement of the part at the build location, and (4) volumetric layer measurement. While the manufacturing process presented in this article (DIW) is not the same as that considered in Grasso et al. (powder bed fusion), their article properly captures the different levels of complexity to consider when creating an *in situ* process monitoring method.[12]

Of the *in situ* monitoring methods presented above, perhaps the most easily implemented approach for direct part measurement is machine vision – an image-based inspection method which has been widely employed in industry for process monitoring and part qualification.[16] Considering the relatively low cost of high-resolution cameras compared to CT scans and ever-improving image processing techniques for region segmentation and object identification, machine vision offers an accessible route to qualify parts with only minor process modifications required to start acquiring data. If images are taken on a layer-wise basis, the measurement technique would be a level 1 measurement method.[12] Thus far, machine vision techniques have been primarily integrated into additive manufacturing processes for defect detection and possible correction of labeled defects.[17–25] Recently, Petsiuk et. al developed a remarkable machine vision technique to inspect a single-component, FFF-printed part for defects where they were able to monitor the process on a layer-by-layer basis and provided strategies to correct the defect.[18] Another article by Sitthi-Amorn et. al detailed a machine-vision assisted 3D printing platform which supported multicomponent printing and even incorporated optical coherence tomography to retrieve high-resolution height information.[19] While both of these processes are able to reconstruct models of the parts that they observed, their intended use focused on part inspection for defect analysis rather than the accuracy of the reconstruction. The accuracy of the reconstructed part is critical if part acceptance is to be based on measurements of internal features.

While machine vision cameras can efficiently capture high resolution images of each printed layer, they often have difficulty distinguishing between printed material and void space. Any gaps in the printed layer serve as windows into the underlying material, which is typically the same shade/color. Although such defects may be detectable "by eye," the actual intensity variations are often too small to be properly classified by machine vision algorithms. In this work, we circumvent this challenge by combining traditional machine vision with profilometry to collect both an intensity and height map of each printed layer. The height map clearly discriminates between regions where new material has been deposited and where it is absent, while the intensity map allows discrimination between visually dissimilar regions. This approach combines the benefits of machine vision (speed, ease of integration) and X-ray CT (identification of internal voids and defects) to yield low-resolution volumetric reconstructions of the printed part without time-consuming post-print inspection.

In this paper, we describe the design of the system and the image processing pipeline that we have developed to produce these reconstructions. Then, we put the new approach to the test in a side-by-side comparison between the as-designed part, the as-manufactured part, the reconstruction generated by our image processing technique, and an X-ray CT scan. This comparison will serve to highlight the advantages and disadvantages of our proposed technique.

2. METHODS

2.1. MATERIALS SELECTION AND PREPARATION

Materials for this article were selected to highlight the unique advantages that layer-by-layer image collection would have in comparison to a traditional *ex situ* technique (such as an X-ray CT).

X-ray CT scanning techniques can differentiate materials based on their X-ray mass attenuation coefficients which can be roughly related to density and nuclear cross sections.[26] To highlight advantages that an *in situ* inspection technique may have over CT scanning, the materials we have used in this study are roughly the same composition and are only visually distinguishable. They can be seen as surrogates for chemically unique formulations that have similar X-ray attenuation coefficients but are visually distinct.[27,28] It is important to note that this case study does not intend to create a one-for-one replacement of CT scanning, rather it is to show an alternative, in-line method to collect data about a part and the manufacturing process.

DOWSIL SE 1700 (Dow, Inc.) silicone was selected as the printing material. The material was dyed either blue or red using SilcPig pigments (Smooth-On). Prior to printing, SE 1700 parts A and B were combined with dye in a 2.5 fl oz reservoir (Nordson EFD) and mixed using a resonant acoustic mixer (Resodyn LabRAM IIH). A sample profile for the mixing cycle can be seen in Figure S1. To prevent the material from heating up and curing during the mix cycle, the cartridge was placed in a custom, water-cooled fixture. During mixing, the cartridge was evacuated to remove any trapped air. Once the SE 1700 was completely mixed, it was spun down in a planetary centrifugal mixer (FlackTek DAC 600.2 SpeedMixer) to remove any remaining air pockets. Lastly, a piston was added to the reservoir prior to being loaded into a cartridge retainer system, mounted to the 3D printer, and pressurized.

2.2. DESIGN OF A MULTICOMPONENT PART

A custom test article was designed for this study with discrete regions of differently colored materials. The primary goal was to demonstrate the ability of our *in situ* data collection and reconstruction techniques to identify features which were only optically accessible during fabrication. From the exterior, the test article is an uninteresting (uniformly blue) cube measuring 35 mm on a side, but inside are embedded shapes intended to test various aspects of the reconstruction technique: two 45-degree angled rings, a spherical shell, and a Lawrence Livermore National Laboratory (LLNL) logo (Figure 1b). The angled rings (2.5 mm thick) can be used to evaluate the vertical reconstruction with respect to angled features, the spherical shell (2 mm thick, 25 mm inner diameter) tests the ability for the reconstruction to segment rings/disks of varying diameter in the layer-wise direction, and the LLNL logo features small spaces (~0.5 mm wide) which will test the processing code's ability to resolve small gaps (as well as the printer's ability to create them). Provided the printer produces the part correctly, the reconstruction should contain all three major features. Identification of these features and their quality in comparison to the actual part will be used to evaluate the quality of the reconstruction.

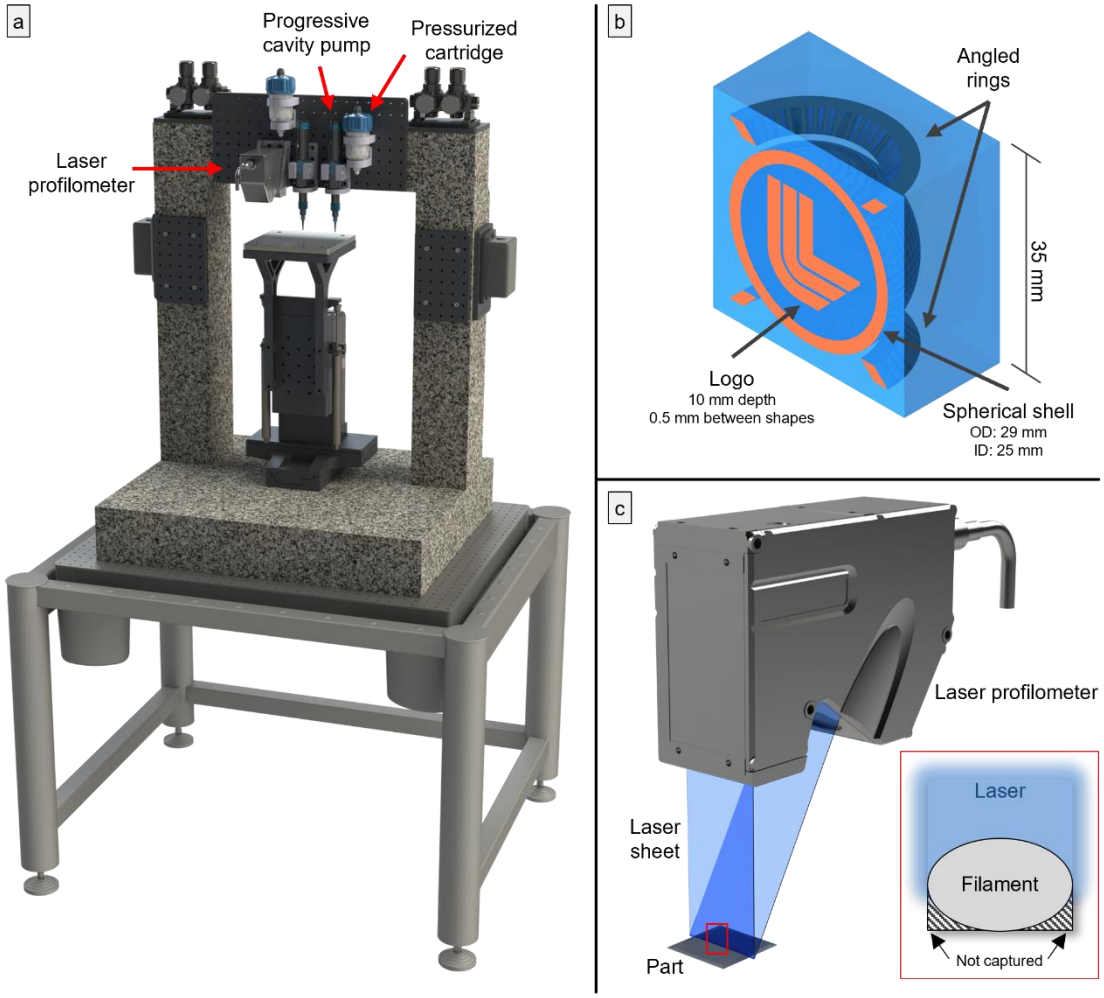

Figure 1: (a) Custom printer setup used to fabricate test articles. (b) Image of test article model (cut in half) showing the main features of interest and relevant dimensions. (c) Depiction of the laser profilometer scanning over a the first layer of a printed part. It is important to note that a whole layer is printed prior to a 3D scan being captured with the laser profilometer. Red bounding box shows what regions of a filament that are captured by the laser profilometer.

2.3. PRINTING PROCESS

The multicomponent test article was 3D printed via a direct ink write (DIW) process on a custom-built 3D printer (Figure 1a). The 3D printer utilizes an Aerotech ANT130XY assembly for the X and Y axes and an Aerotech ANT130LZS stage for the Z axis. The three axes are driven by a trio of Aerotech DP32020E servo drives housed in an Aerotech Npaq drive rack and controlled via PC using the Aerotech A3200 software motion controller. Both axis motion and material dispensing are controlled using Aerotech AeroBasic commands, the latter encapsulated in LLNL's custom flow controller *MoSyFlow*.[29] Material is pressure-fed from the cartridges to the inlet of a progressive cavity pump (ViscoTec preeflow eco-PEN450) which is used for fine control of material flow rate and start/stop. At the outlet of the dispenser is a 0.84 mm inner diameter (18 gauge) Luer lock tapered nozzle (Nordson EFD). The toolpath for the test article was generated using commercial slicing software (Simplify3D) and post-processed for compatibility with the printer and *MoSyFlow* flow controller. Prior to printing, the X, Y, and Z offsets between the two nozzles are measured and a start/stop calibration routine is run to ensure proper extrusion timing parameters are used to minimize defects in the part.[29] The toolpath designed for the test article has a 35 mm/s nominal printing speed, a 0.84 mm filament diameter, and a 0.5 mm layer height (70 layers total). At the completion of each layer, a block of code is executed that moves the stage beneath

the laser profilometer, triggers data collection while moving along a measurement path, and then resumes the print. Once the print is completed, the part is cured in an oven at 150°C for 30 minutes. The total print time of the article was 72 minutes (including 12 minutes of inspection movements).

2.4. IN SITU DATA COLLECTION TECHNIQUE

A data collection routine has been incorporated into the printing process by taking 3D laser profilometry scans on a layer-by-layer basis. A Keyence LJX-8002 controller unit is connected to a Keyence LJX-8080 line-scanning profilometer head that is mounted to a breadboard on the printer using a custom fixture (Figure 1a). The LJX-8080 uses a 405 nm laser sheet that is projected along a 40 mm line and observed using an angled CMOS sensor to triangulate the height of the part (Figure 1c).[30] To collect 3D data, a part can be moved under the profilometer head at a constant velocity using a linear translation stage and multiple profiles can be stitched together to form a 3D surface. In addition to the height data, a grayscale image is produced using the scattered intensity of the laser. Custom parameters have been set in the profilometer controller software to optimize sensitivity of the profilometer and reduce noise in the height image. The profilometer head has a XY-resolution of 12.5 µm and a Z-resolution of 1.25 µm.[30] Data is collected at 500 lines/s while the printer stage is moving at 6.25 mm/s over a 40 mm measurement region (3200 lines total). A full scan takes ~11 seconds/layer using the current parameters and adds ~12.5 minutes to the overall print time (including travel moves). It is important to note that the profilometer is only able to capture the top surface of the part as depicted in Figure 1c. The layer-wise approach to data collection would classify our *in situ* monitoring technique as level 1 per the review article by Grasso et al.[12]

2.5. POSTPROCESSING OF IMAGE DATA AND PART RECONSTRUCTION

The post-processing of the collected height and grayscale data was done in a batch process at the conclusion of the print and involved the convolution of both datasets (section 2.5). The data processing pipeline and images of the data transformation throughout the process can be seen in Figure 2. Postprocessing of the acquired data is done on both the height and grayscale images using a custom Python routine. Readers who wish to familiarize themselves with image processing and machine vision approaches should refer to Steger et al. for complete explanations of algorithms and potential applications.[16]

The layer-by-layer height data is output by the laser profilometer in a 24-bit image format with the height values encoded in the color channel information.[31] The RGB channel information of the bitmap height image encodes 15 bits worth of data – 8 bits green, 3 bits red, and 4 bits blue – which is then combined into a composite value.[31] The composite value is then offset by a reference value for a height of 0 mm (typically half the value of the bit range, 16,384) and multiplied by a constant height factor (c_h) given by equation 1 where h is the height measurement range (41 mm) and b is the bit depth (15).[31] The height factor for our profilometer was calculated to be 0.00125 mm/bit. Prior to any material being printed, the surface of the build plate is scanned and a calculated reference plane is used to adjust the height data by correcting for any misalignment in the profilometer mount.

$$c_h = \frac{h}{2^b} \tag{1}$$

The first step of the segmentation requires the entire image stack to create a convex hull object of the image to reduce the overall amount of data being analyzed (Figure 2c). The guiding principle for data to be included within the convex hull is that the height is above a baseline value and that there is detectable, bright material at those points (to eliminate the influence of reflections skewing height measurements). Prior to creating the convex hull, height data is adjusted by subtracting out any artifacts stemming from angles in the profilometer head mount and orientation to the substrate. Since the distance between the profilometer and top layer is kept constant, the

adjusted height for material above the last layer would nominally be >0 mm and a single height value could be used as a threshold for determining which regions are relevant. The height threshold value for the convex hull image was 0 mm, although this will be adjusted later for material segmentation. A grayscale value of 55 was chosen as the threshold for material presence. It is important to note that the threshold values chosen will impact the resulting part, but it was preferred to use a relatively low grayscale value at this step to maximize the likelihood that all relevant regions of the image were included. The height and grayscale data were subsequently cropped down to the convex hull shape and processed with a separate convolved segmentation process.

Once the global convex hull has been applied, grayscale and height images are separately processed prior to being recombined. Numerous image processing techniques have been employed to overcome difficulties with image saturation, reflections, and light entrapment. Astropy's two-dimensional Gaussian smoothing algorithm ("convolve_fft") was applied to the height data to reduce the impact of drop-offs in crevices or noise spikes from reflective regions.[32,33] This is the most computationally expensive portion of the processing pipeline, but recovering the lost data dramatically improved the quality of the reconstruction. Once the height data has been smoothed, the grayscale and height data stacks are passed to a separate segmentation function. The convolved segmentation function first employs a morphological erosion function to the grayscale image to reduce the number of saturated regions stemming from reflective surfaces.[34] Computational inpainting [35] was also explored as a method to eliminate the bright regions in images, however, it was found that this process was very time intensive compared to erosion (which is the main method used by the profilometer manufacturer to overcome similar artifacts[30]). The grayscale image is then passed through a function to remove small noise and height spikes (notably for regions beyond the perimeter of the part) and a convex hull is computed to represent all the data in the current layer being analyzed.[34]

After applying image correction techniques to the grayscale data, the processed image is then segmented using a multi-Otsu threshold method.[34] Threshold values for the different compositions were chosen by a user to roughly correspond to local minima in values on a histogram of grayscale intensity data (see example histogram in Figure S2). Each pixel in the part is assigned a "material label" corresponding to the Otsu threshold bin number. Minor corrections to the compositional image are applied to remove small holes and objects in the image below an empirically determined size.[34] The compositional map is then convolved with the height data by element-wise multiplication such that only parts above a certain height threshold and with a valid assigned composition value are included in the final data stack. The part is ultimately represented as an evenly spaced voxel grid dataset with each pixel given a value assigned to a specific material.

There are numerous portions of this *in situ* inspection implementation that could be improved which we would like to discuss briefly. Perhaps most notably, there is an inherent difficulty in determining which threshold values for height and grayscale yield results which most closely represent the as-manufactured part. In the case of the parts analyzed here, we have chosen to use a height threshold value that was ~30% of the nominal layer height (0.15 mm). Choosing a threshold height of 0 mm resulted in a significant amount of noise in the height data maps after segmentation, likely due to surface reflections. On the other hand, setting the height threshold to 50% of the nominal layer height excluded a significant amount of material on each layer since there may have been internal material/morphological deformation during part fabrication. Meanwhile, the multi-Otsu thresholding method applied to the grayscale images could have inherent limitations when analyzing parts with more than a few material compositions or in the instances where compositions are similarly colored. One possible alternative to the multi-Otsu threshold which was explored for image segmentation was K-means clustering.[34,36–38] K-means clustering is a machine-learning based technique where data is analyzed and the number/dispersity of apparent "clusters" in the data distribution can be later used to assign values to data points based on which cluster they would belong to.[36–38] This technique proved effective for segmenting the image as a first pass, but was much slower than the multi-Otsu thresholding method for the large-format images using the Simple Linear Iterative Clustering algorithm implemented in scikit-image.[34,37] In the interest of maximizing data fidelity, we have opted to pursue the multi-Otsu thresholding

method, however, future iterations of this effort may incorporate K-means clustering or a different machine learning/artificial intelligence-driven method. A final limitation in the profilometry-based segmentation described here is that it is based on surface measurements but is used to reconstruct a volume.

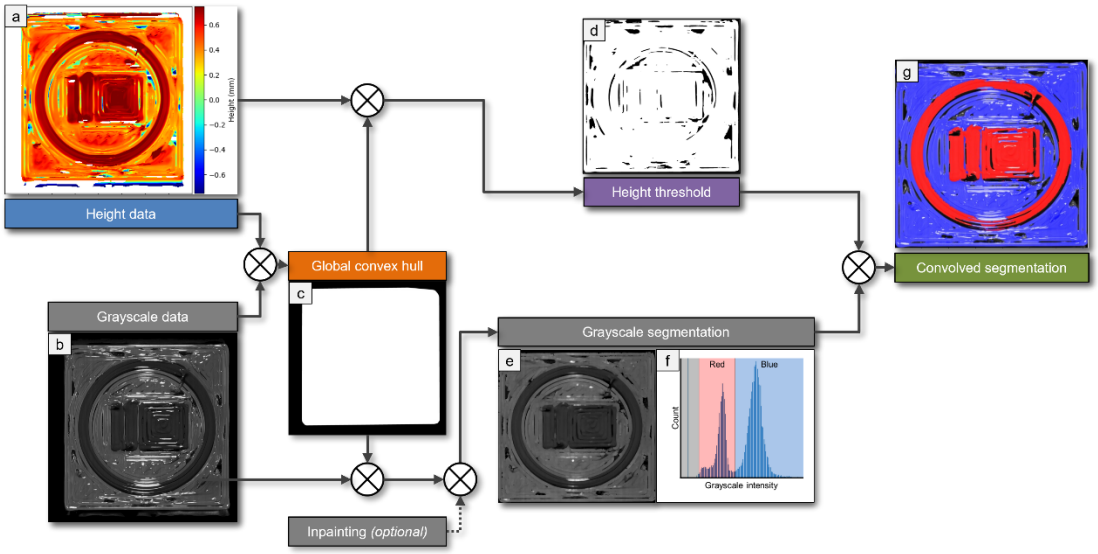

Figure 2: Data processing flow diagram for height and grayscale image convolution. Height data (a) and grayscale data (b) are thresholded and used to create a global convex hull (c) which is applied to every layer to crop down image processing region. The convex hull is then applied to the height and grayscale data on a layer-by-layer basis. Height data is thresholded to create a binary mask (d). Grayscale data is morphologically eroded (e) and segmented using thresholds determined by a histogram (f). Height and grayscale data is once again convolved to get the final layer segmentation (g).

2.6. X-RAY COMPUTED TOMOGRAPHY (CT) OF TEST PARTS

The test article was also analyzed using an X-ray computed tomography (CT) scan. CT scanning is actually a common technique that is used for quality inspection, however, it is natively *ex situ* and data cannot be collected until the part has been completed. After the parts were thermally cured, they were imaged using a North Star Imaging X25 CT scanner at a resolution of 30.08 µm/voxel. It is important to note that CT scans rely on difference in X-ray attenuation to resolve different materials and, since we are using silicones that only differ by color, it is unlikely to see any compositional differences in the captured images.

3. RESULTS AND DISCUSSION

3.1. TEST ARTICLE QUALITY

The test article depicted in Figure 1b was printed using DOWSIL SE 1700 to evaluate the ability for a layer-by-layer inspection technique to properly reconstruct the internal features of a multicomponent additively manufactured part. As discussed in section 2.1, the materials were distinguishable only by their color which were selected to be blue and red for the exterior and interior features of the test article, respectively. After calibrating the flow parameters for the two materials and determining the offset between the two printing tools, the part was printed to completion without any further intervention. As is typical when attempting DIW printing of a nominally full-density article, regions of material under- and over-extrusion were evident and contributed to degraded part quality. In some regions over-extrusion caused the print nozzle to drag through the previously deposited layer and create smearing between distinct regions of the part.

Note, however, that optimization of the print process was not the focus of this work. On the contrary, these imperfections provide an additional opportunity to test our *in situ* diagnostic tool and image processing technique on a range of realistic defects. An image of the exterior of the as-printed part is shown in Figure 3c. The final part has a uniformly colored exterior surface with characteristic ridges on the sides due to the layer-by-layer nature of the fabrication process. There also appears to be regions at the face centers of the cube which are thin walls between the cube exterior and the internal shell exterior. The slicing software placed only small amounts of material in those regions that may not have been optimally dispensed, thus leading to “bleed through” of the color at those faces. From the exterior of the part, it is unclear whether the interior retained its as-deposited morphology, but for the purposes of the image analysis, it is assumed that layers did not significantly change after data had been collected.

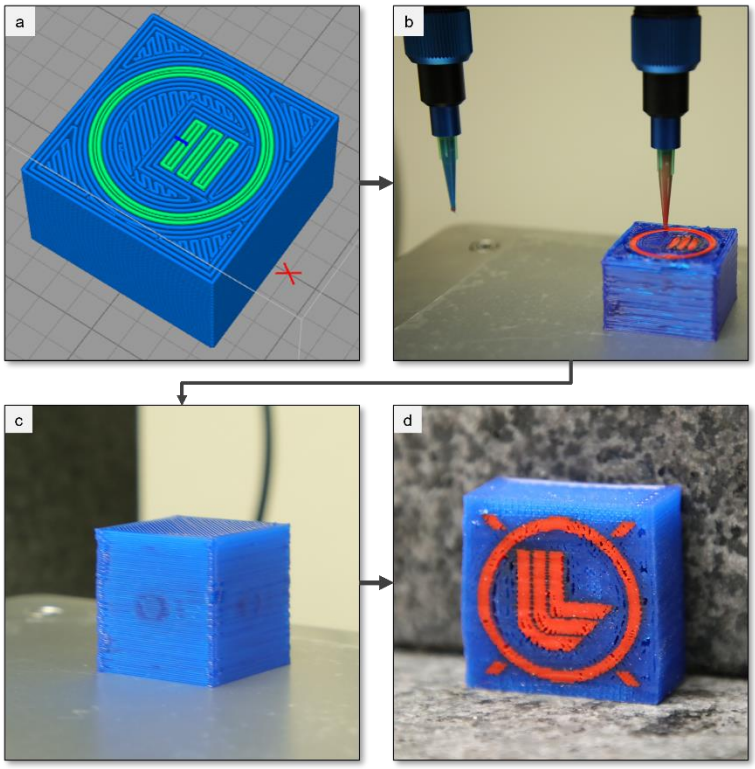

Figure 3: (a) Top-down image of test part in commercial slicing software with full internal filament morphology. (b) Image of the test print at approximately the same location shown in the slicing software. (c) Image of final part exterior after being printed. (d) Image of the part after being bisection in the direction orthogonal to the print.

3.2. LAYER-BY-LAYER GRAYSCALE IMAGES AND HEIGHT MAPS

As discussed in section 2.4, both height and grayscale images were collected on a layer-by-layer basis including a reference image for the baseplate that was used to correct for misalignment of the laser profilometer head. Examples of the raw grayscale images and converted height maps can be seen in Figure 4. These images demonstrate many key challenges that must be considered during image analysis. Looking at the grayscale images of Figure 4 (a1, b1, c1), the two materials are clearly distinguishable in the grayscale images of the part in regions that have both components and can be easily segmented using the relative light intensity (histogram of processed grayscale intensity data in Figure S2). However, many major challenges in the layer-by-layer imaging technique of these parts are clear in this figure, too. The silicone material is naturally glossy and produces saturated regions in the image that impact the ability for an image segmentation program to properly identify composition. Such saturated regions make it difficult to distinguish whether a bright region is bright due to its composition or specular reflections of a glossy

material. Similarly, there are some regions that may appear darker than others due to shadowing and determining whether those regions are darker because of shadowing or are genuinely different compositions is non-trivial. There are also regions beyond the expected bounds of the part in the grayscale image from scattered light on the sheer faces of the cube. Section 2.5 details the methods that were employed to account for these challenges in the 3D reconstruction using data convolution.

Height maps of each layer were captured using the laser profilometer and recorded images are converted to height maps as discussed in section 2.5. Examples of the raw height maps can be seen in Figure 4 (a2, b2, c2). The maximum measurement range of the laser profilometer is +/- 20.5 mm, however, the region of interest has been reduced to mitigate noise on the height measurements for a single layer.[30] Height maps of both single- and multi-component layers capture the filament structure of the part and exhibit gaps in the material where printed filaments may not have overlapped. The retention of this information is vital to determining which material in a grayscale image has been deposited in a new layer and what information can be discarded when segmenting the part for reconstruction. Further voxelization of this information is also pertinent to part reconstructions which retain the wiry interior. A closer look at Figure 4 reveals another challenge with data collection and post processing of these images to recreate a 3D figure stemming from the naturally occurring filaments. The laser profilometer operates by projecting a 1-dimensional line down at the surface and imaging the light at 35° angle relative to the surface; based on the location of the laser line in the 2-dimensional image, the height at a specific point can be calculated by triangulation.[30] However, at the interfaces of multiple filaments, it is possible for light to be projected into the region between the two filaments and not be reflected into the sensor, thus leading to data dropouts in crevices. It is also possible that reflections of the laser off the glossy silicone surface could be misinterpreted and captured as part of the single layer profile. Both scenarios are depicted in Figure S3. Many of the difficulties in data collection and analyzing have been largely solved with a post-processing code (discussed in section 2.5). Despite the challenges in processing the data, it is important to note that the grayscale images alone would not be suitable for accurate volumetric reconstruction of the part as material deposited in previous layers is visually indistinguishable from newly deposited material. Similarly, processed height data would not reveal any information about the internal composition of the part.

Interestingly, the images collected on the first layer deposited are significantly brighter than the remaining images, possibly due to the proximity of the first layer to the reflective metal baseplate. As a result, the height and grayscale mapping for the first layer is relatively poor in comparison to that collected throughout the rest of the print. This complication will be addressed in future iterations of this methodology by using a nonreflective baseplate or temporary adjustment of the illumination settings for the profilometer on the first layer.

The time required to collect data after each layer was ~6.4 seconds/layer. However, when accounting for traveling moves to and from the inspection region the total time added was closer to ~11 seconds/layer. The overall time added to the print (including a single baseplate scan and 70 layers in the part) was ~12.5 minutes. Should the analysis program be added in-line for real-time detection of defects and assessment of part quality, the total manufacturing time might increase even more.

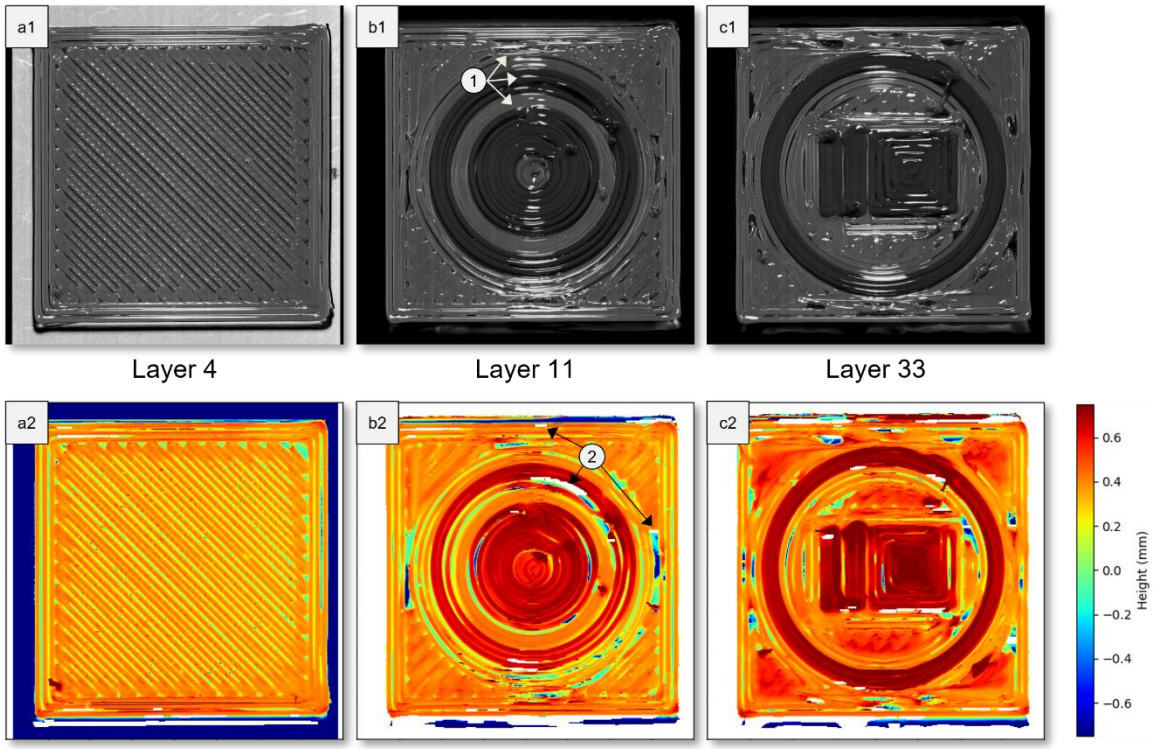

Figure 4: Example images of the layer-by-layer data collected by the laser profilometer at different heights. Surface reflections from the laser appear as bright/saturated regions in the grayscale images. (a1, a2) Layer 4 images showing a single-component slice with the plate in the background. (b1, b2) Layer 11 data showing the level of contrast between the two materials tested. Examples of saturation from light reflections are noted by label 1. Drop-offs of height data in crevices can be seen in the outer ring of b2 (noted by label 2). (c1, c2) Layer 33 data showing the prevalence of saturated regions in the image that complicate segmentation. Grayscale histogram information can be seen in Figure S2.

3.3. VOLUMETRIC PART RECONSTRUCTION AND COMPARISON

The primary goal of this work is to demonstrate that an *in situ* inspection method can be effectively employed on a layer-by-layer basis to create an accurate volumetric reconstruction of an additively manufactured part. The main features of the test article being inspected are an LLNL logo within an embedded spherical shell and the two exterior angled rings on the top and bottom of the shell (see section 2.2 and Figure 1).

The test article that was examined for this work was cut with a razor roughly halfway through the part to serve as a direct comparison between the other inspection methods presented here. It is important to note that the main emphasis for this work was not optimizing the quality of the print, but rather demonstrating that the inspection methods fielded here are able to digitally reconstruct the part and recover the major morphological features. The bisected part has exemplar defects that would be of primary interest when qualifying an additively manufactured part (notably voids and displacement of material). The top and bottom few layers of the part have periodic gaps between filaments remnant of the full density rectilinear infills. There are also gaps between some major filaments and features in the part that are likely traceable to the toolpath itself. The last major defects can be seen between the “L”s in the LLNL logo where it appears that some material was over-extruded and bridged the gaps between the different features.

In addition to having images and profiles collected on a layer-by-layer basis, the printed test articles were also examined using X-ray computed tomography (CT) scans after they had cured. An image at roughly the same location of the part bisection can be seen in Figure 5c. Whereas the CT scan is clearly able to recover the filament-driven features of the part (e.g., holes, gaps) and

has close resemblance to the test article, the density matched materials were not able to be resolved in the images.

An image of the stacked layer data from the profilometry-based part reconstruction can be seen in Figure 5d where colored regions represent different materials and are overlaid on the stacked grayscale images. The primary features of interest are clearly present in the volumetric reconstruction of the part. More importantly, however, the profilometry-based reconstruction captures many of the morphological features that are present in the CT image and the compositional defects in the bisected part. As can be seen in the top of Figure 5d, the periodic filament gaps from the rectilinear infill are present in the reconstruction and closely resemble those shown in the bisected part and CT scan. There are also major gaps in the areas just outside of the spherical feature that are common across all three images. The over-extruded regions in the central logo which led to bridging of the differently colored regions are also loosely captured in the image-based reconstruction. To compare the volumetric reconstruction and CT image, the CT data was segmented and used to estimate the as-printed part volume. The total volume of the part estimated by the CT image was 34.98 cm^3 whereas the estimated volume from the profilometry-based data was 36.50 cm^3 (assuming a 12.5 µm x 12.5 µm x 500 µm voxel size); the difference in estimated volume is <5% and is relatively small (< 2 cm^3).

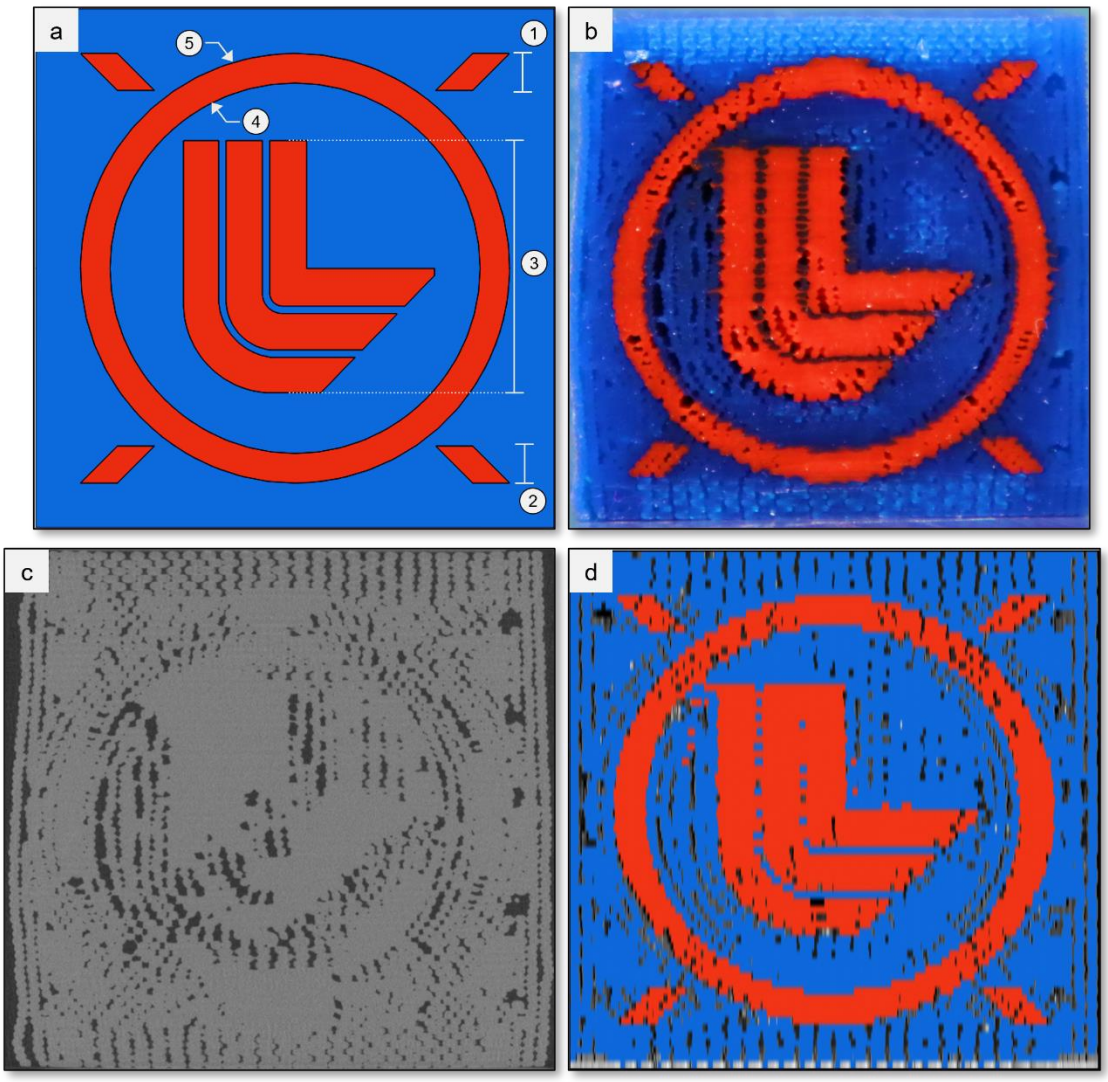

Figure 5: Cross sectional images (slices) of the 3D printed test article. All slices are from the same part and were taken at approximately the same position. (a) Slice of the original CAD model showing design intent.

(b) Photograph of the physical part after bisecting with a razor blade. (c) Slice from the X-ray CT reconstruction of the part. (d) Slice from the laser-profilometer-based reconstruction of the part. Labeled features in (a) are used to compare the measured dimensions between the 3D model, bisected part, and digital reconstruction.

For a more quantitative comparison of the reconstruction to the target and actual parts, five of the features embedded in the part were measured: (1,2) the height of the top and bottom angled rings, (3) the height of the LLNL logo, (4) the vertical and horizontal diameters of the inner spherical shell surface and (5) the vertical and horizontal diameters of the outer spherical shell surface (see Figure 5a). The dimensions provided for the target part (Figure 5a) are measured directly from the 3D model, and the dimensions for the actual part and reconstruction (Figure 5b,d) were measured using ImageJ.[39] The measurements for the reconstruction were rounded to the nearest 0.5 mm in the vertical direction and 0.1 mm in the horizontal direction to account for voxel resolution. The results (provided in Table 1) show that the measurements between the digital reconstruction and the actual part are in relatively good agreement with each other and deviate only slightly from the target dimensions. Deviations in these values could be caused by material shifting during the print after deposition or during the curing process. Notably, the height measurements for the features in the actual part are slightly smaller than those measured for the reconstruction and thus suggests some internal collapse of the material during the print. Future work could focus on reconciling these differences to reduce the difference between these values.

Table 1: Measured dimensions of features in the cross-sectional images displayed in Figure 5.

Region	Description	3D Model	Actual Part	Reconstruction
1	Top angled ring, height (mm)	2.5	2.55	2.5
2	Bottom angled ring, height (mm)	2.5	2.48	2.5
3	Logo height (mm)	17	17.28	17.0
4	Inner shell, vertical diameter (mm)	25	24.08	25.5
	Inner shell, horizontal diameter (mm)	25	25.37	25.2
5	Outer shell, vertical diameter (mm)	29	28.09	29.0
	Outer shell, horizontal diameter (mm)	29	29.86	29.6

Although this reconstruction represents a major accomplishment and offers a path forward for real-time inspection of AM parts, it is not without its drawbacks. One major drawback that was immediately present when directly comparing the CT images and the reconstruction was the possibility that filaments and materials can shift after data has been acquired. As an example, as more mass is added to the part during the print, some of the filament gaps which may have been present in the lower regions could seemingly collapse since the materials are still flowable until they are thermally cured. This morphological evolution can be most clearly seen when examining the lower regions of the digital reconstruction and the CT images. When measuring the overall height of the parts using the CT images in ImageJ [39], we found the actual height to be ~34 mm whereas the target height was 35 mm. Beyond the morphological changes that could be driven by internal stresses during the print, it is also possible that filaments could shift during the thermal cure process.[40,41] These morphological changes were explored by Plott and Shih using a different elastomer system, but their work highlights the inherent difficulty there is when trying to reconstruct parts using data collected on an evolving process. In the future, this could be overcome by using an ultraviolet-cured material system since material would be effectively frozen in place.[41] Another drawback of this method is the loss of data on the under-side of the filaments when taking top-surface topological measurements. The extruded filaments have an elliptical cross section, however, only the top rounded surface is captured (see Figure 1c). For the purposes of this article, the digital reconstruction assumed square voxels spanning the whole layer height (0.5 mm). It is proposed that the relative symmetry of the filaments along their center axis could be used to recover individual filament morphology more accurately (see Figure S4). This effort is reserved for future work as it would require consideration for material shifts spanning the whole build time.

Despite these difficulties, *in situ* characterization of additively manufactured parts via layer-by-layer profilometry measurements and convolved image segmentation could be used as an effective process monitoring and volumetric reconstruction tool. The data analyzed here was

collected in a direction orthogonal to the way it is presented in Figure 5d, yet the digital reconstruction is in good agreement with bisected part and CT image. Looking ahead, any data collected and analyzed in real time could be used to inform a “go/no go” control program that could stop a process if it has too many defects (compositional or morphological) compared to the desired toolpath. Information collected via this technique could be related back to toolpaths and used to inform users and models on how to better control material extrusion to minimize defects. Another potential application of this application could be real-time defect correction based on information gathered by the sensor.[18,19] By creating a volumetric reconstruction of the part in real time, execution of the printing commands could be temporarily paused while a slicer (like ORNL 2) quickly generates toolpath instructions to correct for defects.[42] The section below explores the capability for this *in situ* inspection method to accurately capture defect morphology in the printed part.

3.4. LAYER-WISE VOID COMPARISON

While Figure 5 and Table 1 show agreement between the CT images, bisected part, and laser profilometer reconstructions for the embedded features, we also wished to evaluate defects in the part. Since voids are one of the most common defects in additively manufactured parts and something that our new technique is uniquely suited to identifying, we chose to compare the techniques based on the location and size distribution of voids obtained from each reconstruction. A binary labeling algorithm was applied to the CT images and digital reconstruction at approximately the same location in the part to estimate void areas for a given layer.[34] Comparisons of void location and size distribution for two different positions within the part are shown in Figure 6. While there is general agreement further illustrating the utility of our technique, the data also highlights some shortcomings.

In particular, the distribution plot for the profilometer-based reconstruction seems to bias towards smaller void area in comparison to the CT images. We believe that this is primarily caused by the reflective surfaces of the silicones creating artifacts in the reconstruction that effectively cut large void regions into multiple smaller regions. This phenomenon is especially evident when comparing Figure 6a and Figure 6b, where many of the long diagonal voids that appear continuous in Figure 6b are broken into multiple shorter voids in Figure 6a. The overall area of the voids based on the collection method is also presented in Figure 6c and Figure 6f. The estimated profilometer void area was consistently smaller than the void area estimated using the CT data, although the apparent difference is relatively small in comparison to the area of the single slice. In the most extreme case (Figure 6f), the 50mm^2 difference in void area represents a ~7% difference in the total area of the layer (35 mm x 35 mm, 1225 mm^2). This difference is also consistent with the estimated difference in the volumetric measurements (~5%, see Section 3.3).

It is important to note that comparing these sets of data is inherently difficult and could also partially skew results. The CT data is collected after the material has been cured and there is evidence to suggest that the material may have shifted either after the deposition process or during curing (see the compressed lower section of Figure 5c). Registration of these images and the data is also difficult since the collection methods yield different image resolutions and the objects have significantly different spatial orientations. The disparity of the data collection time and method likely contributes to the apparent differences in the estimated void size distribution plots and area. It is believed that a more direct comparison of these two methods could be carried out with a true *in situ* X-Ray CT scanning method in future studies. It would also be of interest to analyze the overall pore size morphology and distribution, however, the resolution of the data presented herein makes this analysis computationally expensive and thus we have chosen to focus on layer-wise analysis for this comparison. The layer-wise analysis is also more akin to what a human or autonomous process operator would monitor and utilize to make decisions in real-time.

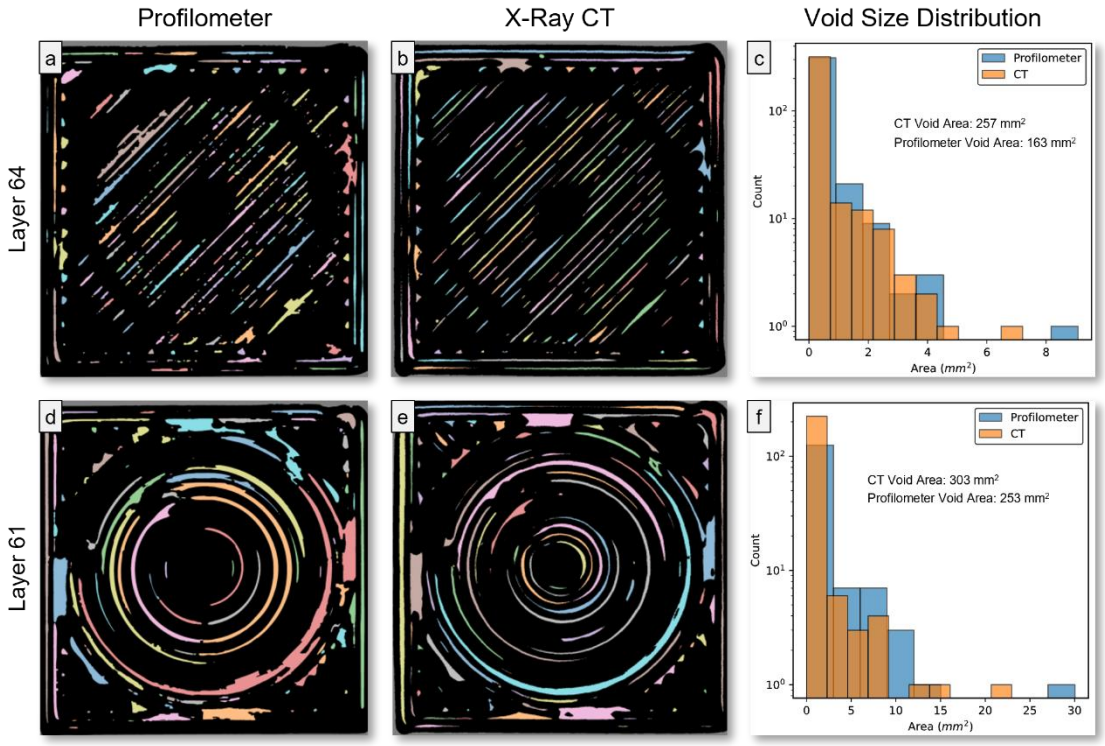

Figure 6: Layer wise comparisons of the profilometer (a, d) and X-Ray CT (b, e) data at two different heights in the test article. Morphological data in the images is shown in the void size distribution plots along with the estimated total area of the voids in the image (c, f) Colored regions in the plot represent "voids" in the layer where it was determined that no material was deposited. The different colors merely serve to highlight distinct regions, and the colors are arbitrary and do not correspond between the profilometer data and CT data.

4. CONCLUSIONS

A layer-by-layer, laser profilometry-based *in situ* characterization technique has been fielded on the direct-ink-write fabrication of a multimaterial part with density-matched, visually distinct materials. The inspection technique yielded height maps and grayscale images which were then analyzed using a custom-built convolved segmentation routine to digitally reconstruct the part. The combination of height data and grayscale images allows this technique to identify both voids (absence of material) and material type when the materials used are visually distinct. In contrast, *ex situ* X-ray CT was able to identify the voids, but could not distinguish between the two materials because of their similar attenuation. Furthermore, the profilometer-based reconstruction is derived entirely from data collected during fabrication and could in principle be computed and analyzed in real time to detect defects on the fly. Both techniques were compared to a physical cross-section of the article and showed excellent agreement.

There were also notable deviations between the profilometer-based (real time) reconstruction and the X-ray CT. Imaging artifacts caused the profilometer-based technique to identify more small voids than the CT. We also observed deviations related to material settling after it was printed, an unavoidable challenge when working with slow-curing ink formulations. Because of this, the profilometer-based reconstruction method is clearly not a one-for-one replacement for X-ray CT analysis if the exact answer is desired. However, a profilometer-based reconstruction can be created with minimal impact to production time and yields information that could be made available for in-line decision making in a way that X-ray CT techniques cannot. This method is also likely adaptable to other forms of additive manufacturing so long as the materials or regions of interest are visually distinguishable. We thus believe the technique merits additional development and may

find future applications in process health monitoring and streamlined part acceptance for production environments.

DECLARATION OF COMPETING INTERESTS

The authors declare that they have no known competing financial interests or personal relationships that could have appeared to influence the work reported in this paper.

AUTHOR CONTRIBUTIONS

D.J. Kline: conceptualization, methodology, software, resources, formal analysis, investigation, data curation, writing – original draft, visualization. M.D. Grapes: conceptualization, methodology, software, writing – review & editing. R. Chavez Morales: software, G.C. Egan: conceptualization, methodology. J.D. Sain: Data curation, resources. Z.D. Doorenbos: resources. H.E. Fletcher: resources. E.A. Avalos: resources. B.M. English: resources. V. Eliasson: project administration. K.T. Sullivan: conceptualization, methodology, writing – review & editing, supervision, project administration, funding acquisition. J.L. Belof: writing – review & editing, supervision, project administration, funding acquisition.

ACKNOWLEDGMENTS

This work was performed under the auspices of the U.S. Department of Energy by Lawrence Livermore National Laboratory (LLNL) under Contract DE-AC52-07NA27344. The authors also gratefully thank the LLNL Lab Directed Research and Development (LDRD) project 21-SI-006 for funding of this work. Document release number LLNL-JRNL-830795.

REFERENCES

[1] I. Gibson, D. Rosen, B. Stucker, M. Khorasani, Additive Manufacturing Technologies, Springer International Publishing, Cham, 2021. https://doi.org/10.1007/978-3-030-56127-7.

[2] D. Han, H. Lee, Recent advances in multi-material additive manufacturing: methods and applications, Curr. Opin. Chem. Eng. 28 (2020) 158–166. https://doi.org/10.1016/j.coche.2020.03.004.

[3] D. Kokkinis, F. Bouville, A.R. Studart, 3D Printing of Materials with Tunable Failure via Bioinspired Mechanical Gradients, Adv. Mater. 30 (2018) 1705808. https://doi.org/10.1002/adma.201705808.

[4] A.M. Golobic, M.D. Durban, S.E. Fisher, M.D. Grapes, J.M. Ortega, C.M. Spadaccini, E.B. Duoss, A.E. Gash, K.T. Sullivan, Active Mixing of Reactive Materials for 3D Printing, Adv. Eng. Mater. 21 (2019) 1900147–1900147. https://doi.org/10.1002/adem.201900147.

[5] D.T. Nguyen, T.D. Yee, N.A. Dudukovic, K. Sasan, A.W. Jaycox, A.M. Golobic, E.B. Duoss, R. Dylla-Spears, 3D Printing of Compositional Gradients Using the Microfluidic Circuit Analogy, Adv. Mater. Technol. 4 (2019) 1900784. https://doi.org/10.1002/admt.201900784.

[6] C. Xu, B. Quinn, L.L. Lebel, D. Therriault, G. L'Espérance, Multi-Material Direct Ink Writing (DIW) for Complex 3D Metallic Structures with Removable Supports, ACS Appl. Mater. Interfaces. 11 (2019) 8499–8506. https://doi.org/10.1021/acsami.8b19986.

[7] K.T. Sullivan, C. Zhu, E.B. Duoss, A.E. Gash, D.B. Kolesky, J.D. Kuntz, J.A. Lewis, C.M. Spadaccini, Controlling Material Reactivity Using Architecture, Adv. Mater. 28 (2016) 1934–1939. https://doi.org/10.1002/adma.201504286.

[8] F. Yang, M. Zhang, B. Bhandari, Recent development in 3D food printing, Crit. Rev. Food Sci. Nutr. 57 (2017) 3145–3153. https://doi.org/10.1080/10408398.2015.1094732.

[9] M. a. S.R. Saadi, A. Maguire, N. Pottackal, M.S.H. Thakur, M.Md. Ikram, A.J. Hart, P.M. Ajayan, M.M. Rahman, Direct Ink Writing: A 3D Printing Technology for Diverse Materials, Adv. Mater. n/a (n.d.) 2108855. https://doi.org/10.1002/adma.202108855.

[10] J. Zhang, J. Wang, S. Dong, X. Yu, B. Han, A review of the current progress and application of 3D printed concrete, Compos. Part Appl. Sci. Manuf. 125 (2019) 105533. https://doi.org/10.1016/j.compositesa.2019.105533.
[11] L. Koester, H. Taheri, L.J. Bond, D. Barnard, J. Gray, Additive manufacturing metrology: State of the art and needs assessment, in: Minneapolis, Minnesota, 2016: p. 130001. https://doi.org/10.1063/1.4940604.
[12] M. Grasso, A. Remani, A. Dickins, B.M. Colosimo, R.K. Leach, In-situ measurement and monitoring methods for metal powder bed fusion: an updated review, Meas. Sci. Technol. 32 (2021) 112001. https://doi.org/10.1088/1361-6501/ac0b6b.
[13] R. Bibb, D. Thompson, J. Winder, Computed tomography characterisation of additive manufacturing materials, Med. Eng. Phys. 33 (2011) 590–596. https://doi.org/10.1016/j.medengphy.2010.12.015.
[14] P. Shah, R. Racasan, P. Bills, Comparison of different additive manufacturing methods using computed tomography, Case Stud. Nondestruct. Test. Eval. 6 (2016) 69–78. https://doi.org/10.1016/j.csndt.2016.05.008.
[15] A. du Plessis, I. Yadroitsev, I. Yadroitsava, S.G. Le Roux, X-Ray Microcomputed Tomography in Additive Manufacturing: A Review of the Current Technology and Applications, 3D Print. Addit. Manuf. 5 (2018) 227–247. https://doi.org/10.1089/3dp.2018.0060.
[16] C. Steger, M. Ulrich, C. Wiedemann, Machine Vision Algorithms and Applications, John Wiley & Sons, 2018.
[17] J. Straub, Initial Work on the Characterization of Additive Manufacturing (3D Printing) Using Software Image Analysis, Machines. 3 (2015) 55–71. https://doi.org/10.3390/machines3020055.
[18] A.L. Petsiuk, J.M. Pearce, Open source computer vision-based layer-wise 3D printing analysis, Addit. Manuf. 36 (2020) 101473. https://doi.org/10.1016/j.addma.2020.101473.
[19] P. Sitthi-Amorn, J.E. Ramos, Y. Wangy, J. Kwan, J. Lan, W. Wang, W. Matusik, MultiFab: a machine vision assisted platform for multi-material 3D printing, ACM Trans. Graph. 34 (2015) 1–11. https://doi.org/10.1145/2766962.
[20] A. Malik, H. Lhachemi, J. Ploennigs, A. Ba, R. Shorten, An Application of 3D Model Reconstruction and Augmented Reality for Real-Time Monitoring of Additive Manufacturing, Procedia CIRP. 81 (2019) 346–351. https://doi.org/10.1016/j.procir.2019.03.060.
[21] O. Holzmond, X. Li, In situ real time defect detection of 3D printed parts, Addit. Manuf. 17 (2017) 135–142. https://doi.org/10.1016/j.addma.2017.08.003.
[22] M. Borish, B.K. Post, A. Roschli, P.C. Chesser, L.J. Love, Real-Time Defect Correction in Large-Scale Polymer Additive Manufacturing via Thermal Imaging and Laser Profilometer, Procedia Manuf. 48 (2020) 625–633. https://doi.org/10.1016/j.promfg.2020.05.091.
[23] J.L. Bartlett, B.P. Croom, J. Burdick, D. Henkel, X. Li, Revealing mechanisms of residual stress development in additive manufacturing via digital image correlation, Addit. Manuf. 22 (2018) 1–12. https://doi.org/10.1016/j.addma.2018.04.025.
[24] J.L. Bartlett, A. Jarama, J. Jones, X. Li, Prediction of microstructural defects in additive manufacturing from powder bed quality using digital image correlation, Mater. Sci. Eng. A. 794 (2020) 140002. https://doi.org/10.1016/j.msea.2020.140002.
[25] F. Caltanissetta, M. Grasso, S. Petrò, B.M. Colosimo, Characterization of in-situ measurements based on layerwise imaging in laser powder bed fusion, Addit. Manuf. 24 (2018) 183–199. https://doi.org/10.1016/j.addma.2018.09.017.
[26] D.F. Jackson, D.J. Hawkes, X-ray attenuation coefficients of elements and mixtures, Phys. Rep. 70 (1981) 169–233. https://doi.org/10.1016/0370-1573(81)90014-4.
[27] X. Ma, M. Buschmann, E. Unger, P. Homolka, Classification of X-Ray Attenuation Properties of Additive Manufacturing and 3D Printing Materials Using Computed Tomography From 70 to 140 kVp, Front. Bioeng. Biotechnol. 9 (2021). https://www.frontiersin.org/article/10.3389/fbioe.2021.763960 (accessed April 12, 2022).
[28] M.J. Ford, C.K. Loeb, L.X.P. Pérez, S. Gammon, S. Guzorek, H.B. Gemeda, A.M. Golobic, A. Honnell, J. Erspamer, E.B. Duoss, T.S. Wilson, J.M. Lenhardt, 3D Printing of Transparent Silicone Elastomers, Adv. Mater. Technol. (2021) 2100974. https://doi.org/10.1002/admt.202100974.

[29] M.D. Grapes, MoSyFlow: Motion Synchonized Flow, Lawrence Livermore National Laboratory, 2021.
[30] LJ-X8000 Series User's Manual (3D mode), (n.d.).
[31] LJ-X BMP Image to Height Data Conversion, (n.d.).
[32] Astropy Collaboration, T.P. Robitaille, E.J. Tollerud, P. Greenfield, M. Droettboom, E. Bray, T. Aldcroft, M. Davis, A. Ginsburg, A.M. Price-Whelan, W.E. Kerzendorf, A. Conley, N. Crighton, K. Barbary, D. Muna, H. Ferguson, F. Grollier, M.M. Parikh, P.H. Nair, H.M. Unther, C. Deil, J. Woillez, S. Conseil, R. Kramer, J.E.H. Turner, L. Singer, R. Fox, B.A. Weaver, V. Zabalza, Z.I. Edwards, K. Azalee Bostroem, D.J. Burke, A.R. Casey, S.M. Crawford, N. Dencheva, J. Ely, T. Jenness, K. Labrie, P.L. Lim, F. Pierfederici, A. Pontzen, A. Ptak, B. Refsdal, M. Servillat, O. Streicher, Astropy: A community Python package for astronomy, Åp. 558 (2013) A33. https://doi.org/10.1051/0004-6361/201322068.
[33] Astropy Collaboration, A.M. Price-Whelan, B.M. Sip\Hocz, H.M. Günther, P.L. Lim, S.M. Crawford, S. Conseil, D.L. Shupe, M.W. Craig, N. Dencheva, A. Ginsburg, J.T. Vand erPlas, L.D. Bradley, D. Pérez-Suárez, M. de Val-Borro, T.L. Aldcroft, K.L. Cruz, T.P. Robitaille, E.J. Tollerud, C. Ardelean, T. Babej, Y.P. Bach, M. Bachetti, A.V. Bakanov, S.P. Bamford, G. Barentsen, P. Barmby, A. Baumbach, K.L. Berry, F. Biscani, M. Boquien, K.A. Bostroem, L.G. Bouma, G.B. Brammer, E.M. Bray, H. Breytenbach, H. Buddelmeijer, D.J. Burke, G. Calderone, J.L. Cano Rodríguez, M. Cara, J.V.M. Cardoso, S. Cheedella, Y. Copin, L. Corrales, D. Crichton, D. D'Avella, C. Deil, É. Depagne, J.P. Dietrich, A. Donath, M. Droettboom, N. Earl, T. Erben, S. Fabbro, L.A. Ferreira, T. Finethy, R.T. Fox, L.H. Garrison, S.L.J. Gibbons, D.A. Goldstein, R. Gommers, J.P. Greco, P. Greenfield, A.M. Groener, F. Grollier, A. Hagen, P. Hirst, D. Homeier, A.J. Horton, G. Hosseinzadeh, L. Hu, J.S. Hunkeler, Ž. Ivezić, A. Jain, T. Jenness, G. Kanarek, S. Kendrew, N.S. Kern, W.E. Kerzendorf, A. Khvalko, J. King, D. Kirkby, A.M. Kulkarni, A. Kumar, A. Lee, D. Lenz, S.P. Littlefair, Z. Ma, D.M. Macleod, M. Mastropietro, C. McCully, S. Montagnac, B.M. Morris, M. Mueller, S.J. Mumford, D. Muna, N.A. Murphy, S. Nelson, G.H. Nguyen, J.P. Ninan, M. Nöthe, S. Ogaz, S. Oh, J.K. Parejko, N. Parley, S. Pascual, R. Patil, A.A. Patil, A.L. Plunkett, J.X. Prochaska, T. Rastogi, V. Reddy Janga, J. Sabater, P. Sakurikar, M. Seifert, L.E. Sherbert, H. Sherwood-Taylor, A.Y. Shih, J. Sick, M.T. Silbiger, S. Singanamalla, L.P. Singer, P.H. Sladen, K.A. Sooley, S. Sornarajah, O. Streicher, P. Teuben, S.W. Thomas, G.R. Tremblay, J.E.H. Turner, V. Terrón, M.H. van Kerkwijk, A. de la Vega, L.L. Watkins, B.A. Weaver, J.B. Whitmore, J. Woillez, V. Zabalza, Astropy Contributors, The Astropy Project: Building an Open-science Project and Status of the v2.0 Core Package, \aj. 156 (2018) 123. https://doi.org/10.3847/1538-3881/aabc4f.
[34] S. van der Walt, J.L. Schönberger, J. Nunez-Iglesias, F. Boulogne, J.D. Warner, N. Yager, E. Gouillart, T. Yu, the scikit-image contributors, scikit-image: image processing in Python, PeerJ. 2 (2014) e453. https://doi.org/10.7717/peerj.453.
[35] G. Bradski, The OpenCV Library, Dr Dobbs J. Softw. Tools. (2000).
[36] N. Dhanachandra, K. Manglem, Y.J. Chanu, Image segmentation using K-means clustering algorithm and subtractive clustering algorithm, Procedia Comput. Sci. 54 (2015) 764–771.
[37] R. Achanta, A. Shaji, K. Smith, A. Lucchi, P. Fua, S. Süsstrunk, SLIC Superpixels Compared to State-of-the-Art Superpixel Methods, IEEE Trans. Pattern Anal. Mach. Intell. 34 (2012) 2274–2282. https://doi.org/10.1109/TPAMI.2012.120.
[38] K.A.A. Nazeer, M.P. Sebastian, Improving the Accuracy and Efficiency of the k-means Clustering Algorithm, (2009) 5.
[39] W. Rasband, ImageJ, U Natl. Inst. Health Bethesda Md. USA. (2012) //imagej.nih.gov/ij/-//imagej.nih.gov/ij/.
[40] J. Plott, A. Shih, The extrusion-based additive manufacturing of moisture-cured silicone elastomer with minimal void for pneumatic actuators, Addit. Manuf. 17 (2017) 1–14. https://doi.org/10.1016/j.addma.2017.06.009.
[41] F. Liravi, E. Toyserkani, Additive manufacturing of silicone structures: A review and prospective, Addit. Manuf. 24 (2018) 232–242. https://doi.org/10.1016/j.addma.2018.10.002.
[42] A. Roschli, A. Messing, M. Borish, B.K. Post, L.J. Love, ORNL Slicer 2: A Novel Approach for Additive Manufacturing Tool Path Planning, in: University of Texas at Austin, 2017. https://repositories.lib.utexas.edu/handle/2152/89889 (accessed April 12, 2022).

SUPPLEMENTAL INFORMATION

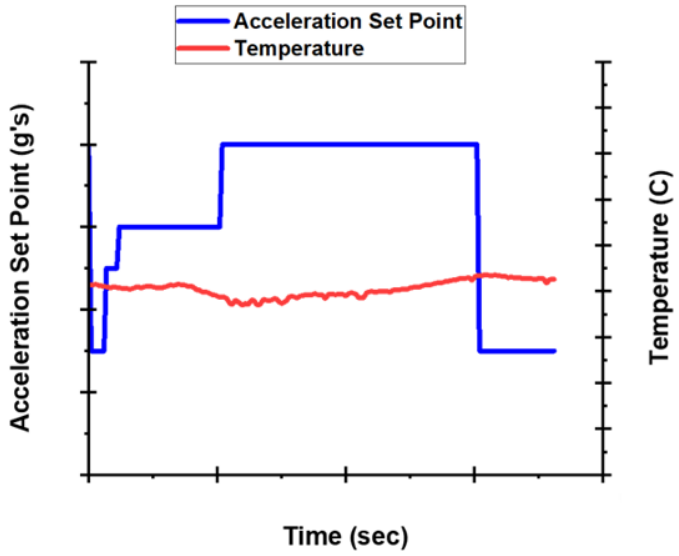

Figure S1: Example mixing profile for DOWSIL SE 1700 mixing on a ResoDyn acoustic mixer along with temperature data for the mixture during the mix cycle. Units omitted.

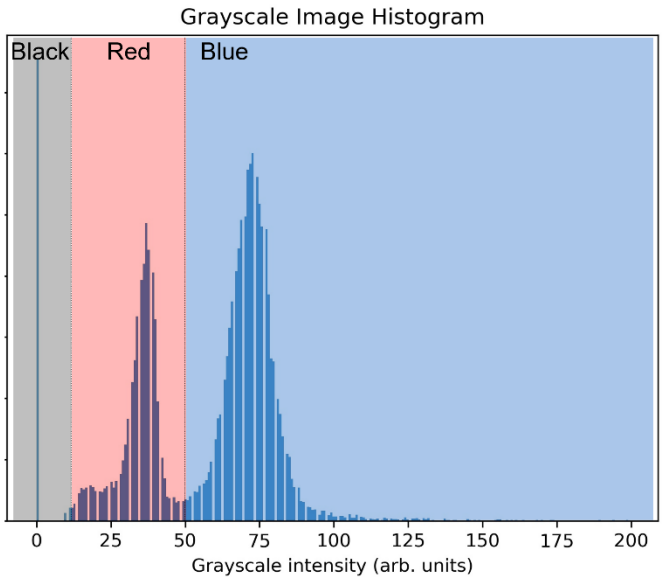

Figure S2: Example histogram of grayscale image data after having performed a morphological erosion. Thresholds for the different material composition are then determined by the user. An example of the different grayscale intensity regions and corresponding material color is overlaid on the histogram.

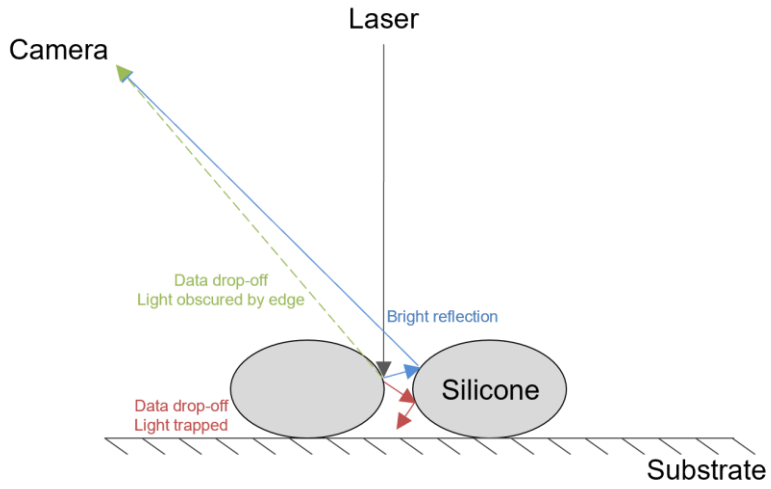

Figure S3: Depiction showing complications with data drop off or light amplification on rounded edges of silicone/glossy filaments.

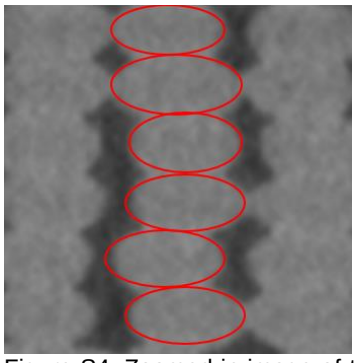

Figure S4: Zoomed-in image of the CT image data presented in Figure 5c highlighting the symmetry of the printed filaments.